*Journal of Sound and Vibration* (2001) **247**(2), 305–323
doi:10.1006/jsvi.2001.3735, available online at http://www.idealibrary.com on IDEAL®

# MINIMIZING THE TRAILING EDGE NOISE FROM ROTOR-ONLY AXIAL FANS USING DESIGN OPTIMIZATION

D. N. SØRENSEN

*Department of Mechanical Engineering, Building* 403, *Technical University of Denmark, DK*2800 *Kgs. Lyngby, Denmark. E-mail: dns@mek.dtu.dk*

(*Received* 18 *September* 2000, *and in final form* 5 *April* 2001)

Numerical design optimization was used to minimize the trailing edge noise of rotor-only axial fans. The design variables were: hub radius, number of blades, rotational speed of the rotor and spanwise distributions of chord length, stagger angle and camber angle. Imposed constraints assured a minimum pressure rise and non-stalled flow conditions across the blades. A blade element model was used to calculate the aerodynamic performance of the fan and, furthermore, provided velocities used in the calculation of the trailing edge noise. Optimizations were made to (1) minimize trailing edge noise, (2) maximize efficiency, and (3) minimize the rotational speed of the rotor. The resulting designs were compared and the potential benefit of minimizing the trailing edge noise was found to be large. Also, the trailing edge noise was minimized while a constraint was imposed on the efficiency. It was found that a considerable noise reduction could be gained with only a limited reduction in fan efficiency. Finally, the dependency of the minimum trailing edge noise on the size of the hub radius was examined. From this, a hub radius existed, for which a minimum trailing edge noise was obtained, and small variations in hub radius could be made with only a limited increase in trailing edge noise.



## 1. INTRODUCTION

In recent years, low noise emission has become a highly competitive factor in the purchase of fan equipment and fan engineers frequently face demands for design of low-noise fans from manufacturers as well as consumers. The noise generating mechanisms are very complicated and a thorough analysis of the sound spectra from a given fan either involves extensive measurements or time-consuming calculations. Instead, most researchers focus on isolating one particular noise generating source and provide guidelines for decreasing the noise level. The *aerodynamic* noise emission may be divided into periodic and broadband types.

The *periodic* (or rotational) noise emission has discrete frequency peaks in the sound spectrum at the blade passing frequency and its harmonics. Some of the major sources of periodic noise emission have been identified as: *upstream obstacles*, e.g., struts or a row of stators, change the magnitude and direction of the flow velocity locally, resulting in varying angle of attack on the rotor. This in turn results in a periodic lift force and the production of a discrete frequency noise emission [1]. Considering fans of the rotor-only type, all upstream influences can be removed by supporting the hub downstream of the rotor. *Downstream obstacles* will be influenced by the wake from the rotor in the same way as

0022-460X/01/420305 + 19 $35.00/0 

discussed for upstream obstacles. For rotor-only configurations, the distance from the rotor to the supporting struts may be increased considerably in order to reduce the velocity-deficit in the rotor-wake and thereby the noise emission. The velocity relative to the (stationary) struts is smaller than the velocity relative to the rotor. Thus, the noise emission from downstream obstacles is significantly smaller than the noise emission from the rotor due to upstream obstacles and a noise reduction may be anticipated by moving struts downstream of the rotor [2]. *Tip clearance eccentricity* was investigated in reference [3] and, especially for small tip clearances, a considerable discrete frequency noise exists at the blade passing frequency. This suggests that constructions with small tip clearances must be accompanied by a very accurate centring of the rotor axis. Furthermore, the duct must be highly circular and all blades of exactly the same length. *Blade irregularities* can cause discrete frequencies below the blade passing frequency if e.g., some blades have an error in the stagger angle setting [4].

The *broadband* noise (or non-rotational) is random in nature and, although not exhaustive, the following sources have been identified as some of the most important: *tip clearance* between blade and outer wall has a large impact on the broadband noise. For rotor axis centered with duct axis, a reduction in tip clearance results in a large decrease in noise emission. Furthermore, an improved efficiency of the fan may be anticipated [3, 5]. A smooth inflow is essential because *turbulence* in the incoming flow results in lift fluctuations which may increase the broadband noise considerably. Furthermore, pressure fluctuations in the turbulent boundary layer on the blade surface may develop noise. Investigations have shown that this noise source is insignificant compared to noise from inflow turbulence and the trailing edge [6]. *Blade stall* will create large fluctuating forces on the suction side of the fan blades, which in turn generates noise [6]. *Trailing edge* noise is caused by the vorticity shed from the trailing edge of the blades which produces local lift fluctuations [7]. Longhouse [8] investigated the possibility of reducing the trailing edge noise by introducing vortex generators on the suction side of the blades.

For both the periodic and broadband noise, the only significant noise generating mechanisms originating from the aerodynamics of the rotor itself, are the blade stall noise and the trailing edge noise. All of the other noise sources mentioned above can be more or less removed by means of carefully manufacturing the blades and duct to remove tip effects, upstream struts, inflow turbulence, etc.

In the present study, a model for the trailing edge noise was combined with an aerodynamical model for rotor-only fans. This resulted in an analysis tool which, for a given rotor geometry and given operating conditions of the fan, provided the trailing edge noise and flow characteristics (e.g., stall properties and pressure rise). The analysis tool was then included in an algorithm for numerical design optimization, which resulted in a tool for finding the fan with the lowest trailing edge noise while constraints ensured a certain pressure rise and non-stalled flow across the blades. The design variables were: hub radius, number of blades, rotational speed of the rotor and spanwise distributions of chord length, stagger angle and camber angle. In reference [9], the aerodynamical model and the optimization algorithm were combined and used in a study regarding optimization for maximum efficiency.

For the minimization of the trailing edge noise by means of numerical design optimization, a reliable, numerically efficient, and robust analysis model for the noise emission is required. Here, the model developed by Fukano *et al.* [7] was chosen. This model has been thoroughly validated against experiments [7, 10, 11] and is adequate for comparing different designs in an optimization process. A similar model for the trailing edge noise is presented in reference [12], where comparisons show that their model is in slightly better agreement with experiments than the model of Fukano *et al.*, probably because the

boundary layer parameters in reference [12] are based on airfoils in cascade, whereas flat plate parameters are used in reference [7]. Combined with an optimization scheme, the same noise prediction model is used to compare different designs. If the model is able to, qualitatively, determine the differences in noise level to variations in the geometry of the fan, the quantitative determination of the noise emission is of less importance. Due to its simplicity and thorough validation, the model from reference [7] was chosen in this work.

Besides a noise prediction model, an aerodynamical model is required to calculate the aerodynamic constraints, posed as part of the optimization problem. Furthermore, the aerodynamical model provided axial and tangential velocities relative to the rotating blade which is required by the noise prediction model. To avoid the restrictions on the radial distributions of the axial and tangential velocities in the often used *free vortex flow* model, the more general *arbitrary vortex flow* model by Sørensen and Sørensen [13] was used.

In reference [14], the trailing edge noise model from reference [7] is used to investigate the potential of noise minimization of axial fans. The cascade method used in reference [14] predicts the axial velocity distribution, which corresponds to a prescribed tangential velocity distribution. Also, the pressure rise is predicted and, by using the velocities, the trailing edge noise determined. By combining these models with an optimization algorithm, the optimum spanwise distributions of tangential velocity is determined. A comparison of measurements of the noise emission for the optimum fan with a fan designed for a tangential velocity proportional to the square root of the inverse radial position, shows that a reduction in noise emission can be obtained [14]. The main differences between the present method and the method proposed in reference [14] is that the aerodynamic model from reference [13] includes losses due to airfoil drag, secondary drag, tip clearance, and downstream diffuser, and therefore enables calculation of the fan efficiency, whereas this property must be postulated in reference [14]. Also, the cascade method used in reference [14] only enables the optimization algorithm to determine the tangential velocity distribution and, afterwards, a suitable planform must be selected. In the present work, the planform was included as part of the optimization problem and was therefore a direct result of the optimization. However, the complexities of the aerodynamical model and the optimization problem in the present formulation is significantly larger than in reference [14], thereby resulting in larger computing times.

In the present work, numerical design optimization was used as a tool to investigate different *optimum* designs. By varying a number of parameters, the numerical results were related to the equations of the models governing the trailing edge noise and aerodynamical characteristics. An investigation was carried out to show the difference between optimizing for (1) minimum trailing edge noise, (2) maximum efficiency and (3) minimum rotational speed of the rotor. The potential benefit of minimizing the trailing edge noise, compared to maximizing the efficiency or minimizing the rotational speed of the rotor was significant. Also, the trailing edge noise was minimized while a constraint ensured a certain efficiency, and a large noise reduction was possible with only a small decrease in efficiency. Finally, the minimum trailing edge noise was found as a function of the hub radius for two different pressure rise requirements. For hub radii near the "optimum" hub radius, with minimum trailing edge noise, the trailing edge noise was only weakly dependent on the hub radius, whereas, far from the "optimum" hub radius, a large increase in trailing edge noise was found.

Finally, it should be noted that the objective function, design variables and constraints were chosen as representative examples. The design method is general and may be altered with other models for the aerodynamics or for the noise emission. Also, other design variables or constraints may easily be introduced.

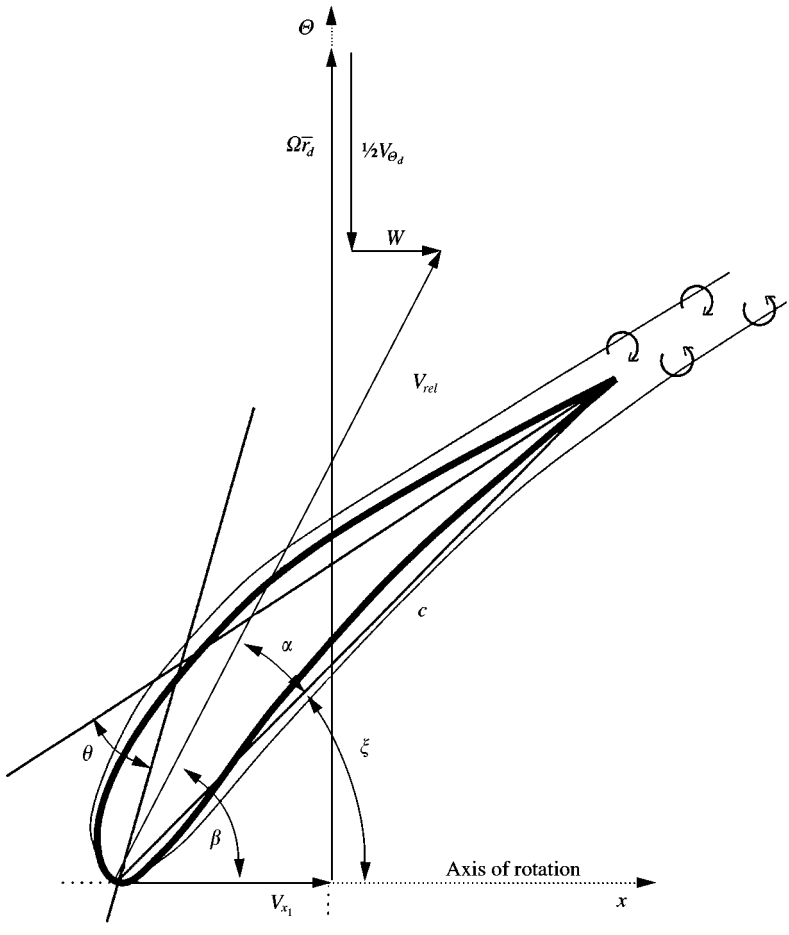


Figure 1. Co-ordinate system showing the rotating blade element and the velocities experienced by the blade element. Furthermore, a sketch of the vortices generating trailing edge noise is shown. Cut in the ($x$–$\theta$) plane (constant $r$).

## 2. METHODS

The models for the fan aerodynamics and for the trailing edge noise both require that the blades of the rotor are divided into a number of spanwise blade elements. In Figure 1, one of the blade elements is depicted with definitions of angles and velocities used in the models. Furthermore, the vortex shedding mechanism from the trailing edge is sketched. After a brief description of the models for the fan aerodynamics and the trailing edge noise in sections 2.1 and 2.2, the numerical optimization problem is defined in section 2.3. Only formulas necessary for the discussions in section 4 are included.

### 2.1. AERODYNAMIC MODEL

The pressure rise and efficiency of the fan were calculated using an aerodynamic model for arbitrary vortex flow fans [13]. Furthermore, the model determined the velocities relative to the blade elements, which were used in the trailing edge noise model.

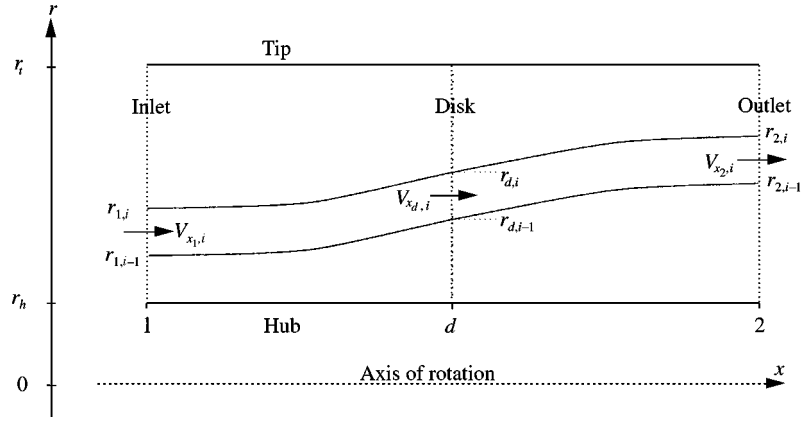


Figure 2. Annulus between hub and tip divided into a number of blade elements.

The model is an axisymmetric, incompressible and inviscid blade element model [13]. The annulus between the hub and tip of the rotor is divided into a number of streamtubes, each containing a blade element, and the flow is assumed to be fully developed and parallel far upstream and far downstream of the rotor (Figure 2). In Figure 1, a blade element with velocities and angles is shown. $N = 33$ blade elements is sufficient for a solution, which is essentially independent of $N$ [13]. In the following, indices 1, $d$, and 2 refers to axial positions far upstream of the rotor disc, immediately downstream of the rotor disc and far downstream of the rotor disc respectively. Index $i$ refers to the $i$th streamtube. The inner and outer edges of the $i$th streamtube are denoted by $r_{i-1}$ and $r_i$ respectively (Figure 2) (a list of nomenclature is given in Appendix A).

The kinematic assumptions for the model are as follows [13]. (1) The *axial velocity* varies continuously from far upstream to far downstream of the rotor disc. The axial velocity at the rotor disc and the outlet are assumed to be $V_{x_d,i} = V_{x_1,i} + w_i$ and $V_{x_2,i} = V_{x_1,i} + 2w_i + w_0$, respectively, where $w_i$ is the axially induced velocity at the rotor disc and $w_0$ is a constant level which applies for all streamtubes. (2) The *tangential velocity* is zero upstream of the rotor. Downstream of the rotor, the circulation is preserved. With the tangential velocity immediately downstream of the rotor disc denoted by $V_{\theta_d,i}$, the tangential velocity is $\frac{1}{2}V_{\theta_d,i}$ at the rotor disc. (3) The *radial velocity* is zero far upstream and far downstream of the rotor and varies continuously. (4) Far downstream of the rotor, the *pressure* comprise a constant level, $p_0$ and a radial distribution, $p_2$. Thus, $p(r) = p_0 + p_2(r)$, where $p_2$ equals zero at the hub radius.

For each streamtube, governing equations are formulated for conservation of mass, conservation of axial momentum, and conservation of tangential momentum. Furthermore, far downstream of the rotor, pressure equilibrium must exist:

$$\left.\frac{\mathrm{d}p}{\mathrm{d}r}\right|_2 = \rho \frac{V_{\theta_2}^2}{r_2}. \tag{1}$$

Finally, global continuity is ensured by integrated mass conservation at the rotor disc and far downstream. The governing equations are coupled due to the pressure equilibrium equation across each streamtube as well as the integral equations for mass conservation (see reference [13] for details).

With the rotational speed of the rotor denoted by $\Omega$, the *relative velocity*, $V_{rel,i}$, experienced by the rotating blade element and the *angle*, $\beta_i$, between the rotational axis and

$V_{rel,i}$ (Figure 1) are determined by

$$V_{rel,i}^2 = \left(\frac{1}{2}(r_{d,i} + r_{d,i-1})\,\Omega - \frac{1}{2}V_{\theta_d,i}\right)^2 + (V_{x_1,i} + w_i)^2, \tag{2}$$

$$\tan\beta_i = \frac{(1/2)(r_{d,i} + r_{d,i-1})\,\Omega - (1/2)V_{\theta_d,i}}{V_{x_1,i} + w_i}. \tag{3}$$

From the rotor geometry and the relative velocity and angle, the axial and tangential forces from the rotor are determined from tabulated airfoil data of the NACA 65 airfoil family in cascade configuration [15]. The tabulated data were smoothed as described in reference [9]. Besides the losses due to airfoil drag, empirical relations are included to model aerodynamic losses from secondary drag [16], tip clearance [17], and downstream diffuser [16]:

$$C_{D_s} = 0{\cdot}018\bar{C}_L^2 + 0{\cdot}02c/(\sigma[r_t - r_h]), \qquad C_{D_{tip}} = 0{\cdot}7\bar{C}_L^2 t/(r_t - r_h), \tag{4, 5}$$

$$\Delta p_D = (1 - \eta_D)1/2\rho\bar{V}_{x_1}^2(1 - (A_1/A_2)^2), \tag{6}$$

where $\sigma$ is the solidity, $c$ the chord, $r_h$ and $r_t$ the hub and tip radii, respectively, and $\bar{C}_L$ the average lift coefficient. The tip clearance is denoted by $t$, $\Delta p_D$ is the pressure loss in the diffuser, $\eta_D$ the diffuser efficiency, $\rho$ the density, $\bar{V}_{x_1}$ the mean throughflow velocity in the annulus, and $A_1$ and $A_2$ the areas of the annulus and the full duct respectively. In the present study, the tip clearance and the diffuser efficiency were fixed at $t = 1$ mm and $\eta_D = 95\%$ respectively. The secondary drag term, $C_{D_s}$ and the tip loss term, $C_{D_{tip}}$ applies to each streamtube and thus enters the iterations of the aerodynamic model as additions to the airfoil drag, whereas the pressure loss in the downstream diffuser $\Delta p_D$ is applied as a correction to the integrated pressure rise across the rotor.

The system of non-linear equations is solved using a Newton–Raphson method and the Jacobian matrix of the problem is sparse which is used to accelerate the solutions. The low computing costs combined with the highly converged solutions make the model suitable for numerical design optimization of ducted rotor-only axial fans.

For each streamtube, the total pressure rise is *defined* as the change in the sum of static pressure and the dynamic pressure from the axial velocity. The dynamic pressure from the tangential velocity cannot be regained in a rotor-only configuration and is not included in the total pressure rise. The *total pressure rise* across the fan, $p_T$, is the summation of the area weighted contributions from each streamtube. The *efficiency* is defined as

$$\eta = Qp_T/P, \tag{7}$$

where $Q$ is the flow rate and $P$ the mechanical shaft power, determined from integrated lift and drag contributions.

## 2.2. TRAILING EDGE NOISE MODEL

The sound pressure level was determined by using the method of Fukano *et al.* [7], modelling the broadband noise generated by the trailing edge vortex shedding of the turbulent boundary layer (sketched in Figure 1). The noise is generated by turbulence, resulting in fluctuations in the pressure around the blade which, in turn, can be attributed to variations in the lift coefficient. These variations stem from alternating vortices being shed when the turbulent boundary layer interacts with the trailing edge of the blade. Fukano

*et al.* [7] showed that the total sound power, $E$, radiated from the rotor may be expressed by

$$E = \frac{B\pi\rho}{1200a_0^3} \sum_{i=1}^{N} D_i V_{rel,i}^6 (r_i - r_{i-1}), \tag{8}$$

where $B$ is the number of blades, $a_0$ the speed of sound, $V_{rel,i}$ the relative velocity (equation (2)), and $D_i$ is the wake width of the $i$th blade element. The boundary layer on each side of the airfoil is approximated with a turbulent, zero pressure gradient boundary layer and the wake width becomes [7]

$$D_i = D_{T,i} + 2(0{\cdot}37/8c_i)\,\mathrm{Re}_i^{-0{\cdot}2}, \tag{9}$$

where $D_{T,i}$ is the trailing edge width of the airfoil and $\mathrm{Re}_i$ the Reynolds number based on $c_i$ and $V_{rel,i}$. The assumption of a zero pressure gradient boundary layer, justifying equation (9), is questionable for cambered airfoils. However, experimental evidence suggests that equation (9) is applicable for camber angles below 20° [10], which was the case in this study.

The sound pressure, $\sqrt{\bar{p}^2}$, can be calculated from the total sound power by

$$E/2 = \left(\frac{4\pi}{3}\right)\left(\frac{d^2}{\rho a_0}\right)\bar{p}^2, \tag{10}$$

where $d$ is the distance from the rotor to the measuring probe. Finally, the sound pressure level, *SPL*, is defined as

$$SPL = 10\log_{10}\left(\frac{\bar{p}^2}{p_{ref}^2}\right), \tag{11}$$

where $p_{ref}$ equals $2\times10^{-5}\,\mathrm{N/m^2}$. In the following calculations of the sound pressure level, $d = 1{\cdot}5\,\mathrm{m}$ and $D_T = 1\,\mathrm{mm}$ were arbitrarily chosen.

It should be noted that the above model estimates the total sound power radiated from the rotor, without considering the actual use of the fan. For ducted fans, however, the duct system imposes restrictions on the acoustic modes that can be propagated. A sound wave in a duct may be decomposed into axial, circumferential, and radial modes. The axial modes (plane waves) are always propagated since they cut-on at 0 Hz. The circumferential and radial modes, however, are only propagated for frequencies above cut-on, as determined by the duct system. An order-of-magnitude estimation of the frequencies emitted from the rotor can be made from the dimensionless Strouhal number, $\mathrm{St}_i = f_i D_i / V_{rel,i}$. Assuming a Strouhal number of 0·2 provides the estimated frequency for each blade element and, since $D_i$ and $V_{rel,i}$ vary along the blade, the broadband frequency range for the fan for a given flow rate [7]. Doing this for a few representative optimum fans from section 3 returns frequencies in the range from 3 to 10 kHz. This is an order of magnitude larger than the cut-on frequency for the first circumferential mode of the duct, and thus most of the sound power emitted from the rotor is able to propagate in the duct system, justifying the use of the relatively simple model described above.

A detailed prediction of the trailing edge noise propagation in the duct system is very hard to obtain, since it is difficult to determine, accurately, the frequencies of the noise emitted because of the interaction of the turbulent boundary layer with the trailing edge of the rotor. Furthermore, calculation of the modal distribution in the duct system, of the multiple frequencies, is a difficult task. One approach to the detailed modelling of broadband noise, propagating in ducts, is presented in reference [18], where Glegg and Jochault modified trailing edge noise levels, measured from isolated blades, to obtain the

in-duct sound power from high-solidity fans. These are then coupled with the modes of a circular duct, resulting in a model for the propagation of broadband trailing edge noise, including modal distribution. In reference [19], measurements of the plane wave as well as the first two circumferential modes show that, when cut-on, the circumferential modes may contain more energy than the plane wave for a given frequency.

### 2.3. FORMULATION OF THE OPTIMIZATION PROBLEM

The standard constrained optimization problem can be formally stated as

$$\text{Minimize } F(\Phi_n), \qquad n = 1, 2, \ldots, NDV, \tag{12}$$

$$\text{subject to } g_j(\Phi_n) \geqslant 0, \quad j = 1, 2, \ldots, NCON, \tag{13}$$

where *NDV* denotes the number of design variables and *NCON* the number of constraints. The *objective function*, $F$, describes the figure of merit of the possible configurations, defined by the *design variables*, $\Phi_n$, which can be altered by the optimizer, to find the minimum of $F$. Finally, the *constraints*, $g_j$, define the geometrical and operational restrictions of the design. If the equality holds for a constraint in equation (13) for the optimum design, the constraint is said to be active.

Below, a description of the objective function, design variables and constraints used in the present study is given. Furthermore, the minimization algorithm is briefly described.

#### 2.3.1. *Objective function*

Three different objective functions were investigated. *Noise*: the purpose of the optimization was to minimize the trailing edge noise, equation (11). *Efficiency*: the optimization was performed with the purpose of maximizing the efficiency, equation (7). *Rotational speed of the rotor*: the optimization was carried out to minimize the rotational speed of the rotor.

#### 2.3.2. *Design variables*

The design variables, defining the possible fan configurations, were the hub radius, $r_h$, the number of blades, $B$, the rotational speed of the rotor, $\Omega$, and the spanwise distributions of chord length, $c(r)$, stagger angle, $\xi(r)$, and camber angle, $\theta(r)$ (Figure 1). The number of blades is a discrete property and could not be included in the chosen optimization scheme. Thus, separate optimizations were performed for different values of $B$. The spanwise distributions of chord, stagger and camber were defined using single-segment Bézier curves with four vertices, distributed evenly from hub to tip. Thus, the optimization problem was described by a total of 14 design variables, except for the investigations in section 3.3, where the hub radius was fixed.

#### 2.3.3. *Constraints*

Requirements from the manufacturer determine the specifications, and thus the constraints, of the fan. These may be due to geometrical restrictions as well as desired properties of the fan. Here, a fan was considered with a fixed tip radius, $r_t = 267$ mm, able to deliver a flow rate of $Q = 4{\cdot}45\,\text{m}^3/\text{s}$ at a pressure rise of either $p_T = 2000$ or 2400 Pa.

The geometrical constraints were: *hub radius*, $r_h$: should be larger than 100 mm. Furthermore, the annulus between hub and tip should be larger than 30 mm. *Chord length*,

$c$: the tabulated airfoil data were restricted to solidities between 0·5 and 1·5. To avoid extrapolations of the data, the chord was constrained to solidities between 0·52 and 1·48, where the solidity is defined as $\sigma = c/s$, with $s = 2\pi r/B$. *Stagger angle*, $\xi$: was kept between 2 and 88 degrees to aid the optimization algorithm in narrowing the possible values during intermediate iterations. *Camber angle*, $\theta$: the tabulated airfoil data were restricted to camber angles between 12 and 18°. To avoid extrapolations, the camber angle was constrained between 12·1 and 17·9°.

The constraints from operational requirements were: *rotational speed* of the rotor, $\Omega$: should be below 3000 r.p.m. *Total pressure rise*, $p_T$: as described above, the fan should be able to deliver either $p_T = 2000$ or 2400 Pa. *Tangential velocity* in outlet: the ratio of tangential-to-axial velocity at the outlet was kept below 1·1 for all streamtubes. This limit was imposed to avoid vortex breakdown downstream of the rotor, a flow-state which cannot be captured by the aerodynamic model, see reference [9] for further details. *Axial velocity* in outlet: the aerodynamic analysis model is unreliable if very small outlet velocities occur and a constraint was imposed to ensure that the axial velocity in the outlet of each stream tube was not less than 0·26 of the mean throughflow velocity [13]. *Stall limit*: at high angles of attack, the flow on the blades may stall, resulting in a large increase in noise emission [6]. In the present work, stall was defined to occur when the lift coefficient reached the maximum value. For each blade element, the angle of attack, $\alpha$, was kept at least one degree below stall. *Efficiency*: was constrained to be above a specific value, $\eta_c$, in the investigations in section 3.2.

#### 2.3.4. *Optimization algorithm*

The optimization problem is differentiable and has non-linear objective function and constraints. The method used for the solution of the optimization problem is a sequential quadratic algorithm [20, 21] which is one of the most efficient algorithms for these types of problems. The algorithm requires gradients of the objective function and constraints with respect to the design variables. These were calculated by finite differences using the central difference scheme. The optimization algorithm does not ensure that the determined solution is a global optimum, and to increase the probability of finding the global optimum, several optimizations with different initial geometries were performed. If different solutions were found, the superior one was assumed to be the global optimum. A detailed description of the implementation of the optimization algorithm is given in reference [22].

## 3. RESULTS

### 3.1. MINIMUM NOISE, MAXIMUM $\eta$ AND MINIMUM $\Omega$

Optimizations were performed to (1) minimize the trailing edge noise, (2) maximize the efficiency, and (3) minimize the rotational speed of the rotor. The design point was $Q = 4{\cdot}45\,\mathrm{m}^3/\mathrm{s}$ and $p_T = 2000$ Pa and optimizations were performed for $B = 4$ up to $B = 28$ blades with a four blade interval. The same geometrical and operational constraints were imposed in all three cases (section 2.3) and the performance capabilities of the fans were identical.

In Figure 3(a), the trailing edge noise for the three types of optimizations are depicted as a function of the number of blades. In Figure 3(b), the corresponding efficiencies are shown and Figure 3(c, d) shows the optimum values of the design variables rotational speed of the rotor and hub radius respectively. Furthermore, for the case of $B = 16$, the geometry of the optimum solutions is shown in Figure 4, which contains the spanwise distributions of

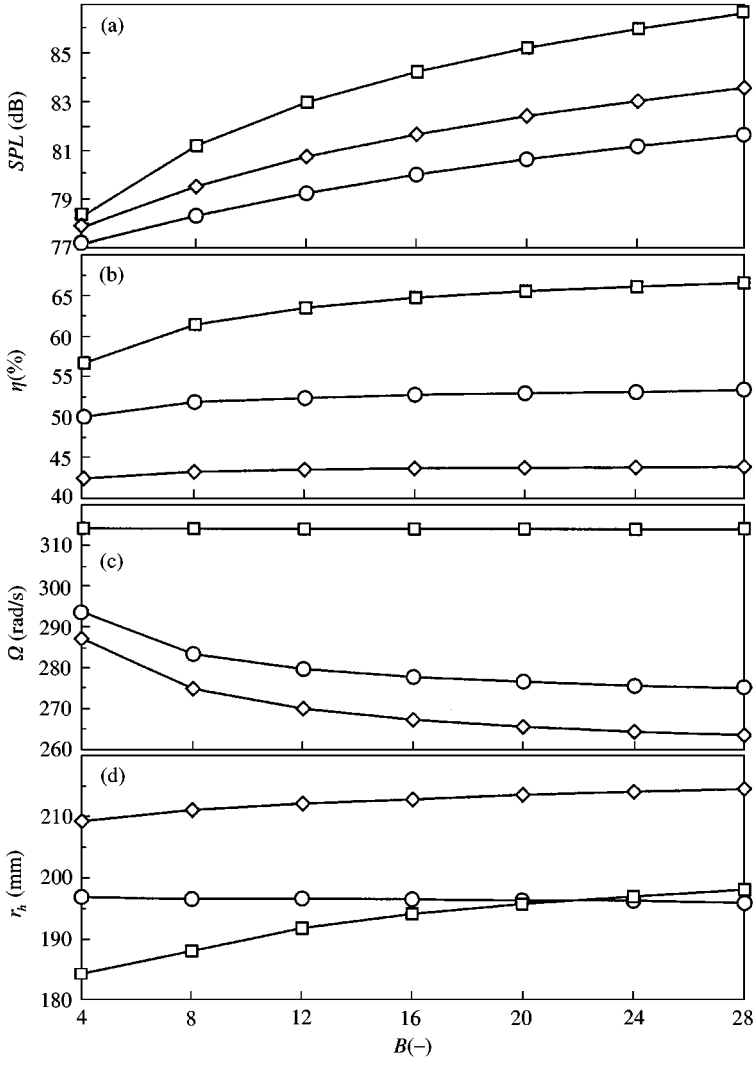


Figure 3. Trailing edge noise (a), efficiency (b), rotational speed of the rotor (c), and hub radius (d) for the optimum designs, $Q = 4{\cdot}45\,\mathrm{m}^3/\mathrm{s}$, $p_T = 2000$ Pa: ○, optimization for minimum *SPL*; □, optimization for maximum $\eta$; ◇, optimization for minimum $\Omega$.

chord (a), stagger angle (b), and camber angle (c). Also, the aerodynamics of the optimum designs for $B = 16$ are shown in Figure 5, containing the spanwise distributions of axial (a) and tangential (b) velocities far downstream of the rotor, and the static pressure rise across the rotor (c).

When the optimizations were performed to minimize *SPL*, the pressure rise constraint and the tangential velocity constraint were active for all $B$. The rest of the constraints were inactive. When the optimizations were performed to maximize $\eta$, the constraint on $\Omega$ and the pressure rise constraint were active for all $B$. Finally, when optimizing for minimum $\Omega$, the pressure rise constraint and the tangential velocity constraint were active for all $B$. For the case of $B = 16$, the spanwise distribution of the ratio of tangential-to-axial velocity in the outlet is depicted in Figure 6 for the three optimum designs.

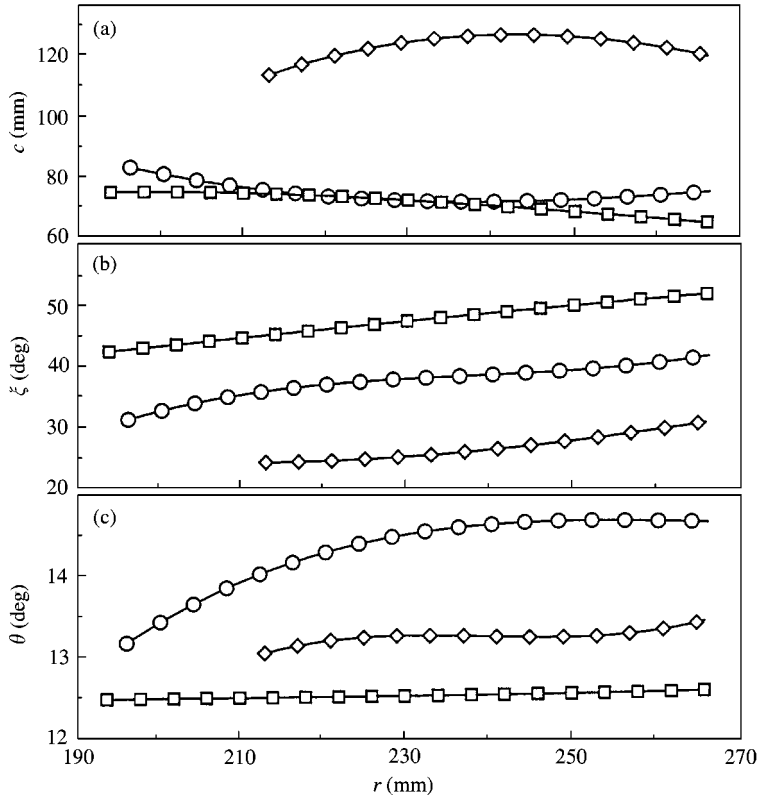


Figure 4. Spanwise distributions of chord (a), stagger angle (b), and camber angle (c) for the optimum designs, $B = 16$, $Q = 4{\cdot}45\,\mathrm{m}^3/\mathrm{s}$, $p_T = 2000\,\mathrm{Pa}$: ○, optimization for minimum *SPL*; □, optimization for maximum $\eta$; ◇, optimization for minimum $\Omega$.

### 3.2. MINIMUM NOISE, CONSTRAINING $\eta$

The trailing edge noise was minimized while keeping the efficiency above a specified value by imposing a constraint, $\eta_c$ on the efficiency. The design point was $Q = 4{\cdot}45\,\mathrm{m}^3/\mathrm{s}$ and $p_T = 2000$ Pa in all cases. Optimizations were performed for four, eight and 16 blades. In Figure 7, the minimum *SPL* is depicted as a function of $\eta_c$. The left endpoint of each of the three curves is from the optimization for minimum *SPL* and the right endpoint from the optimization for maximum $\eta$ (section 3.1). Disregarding the endpoints which were described in section 3.1, constraints were active for efficiency and pressure rise in all cases. The constraint for the tangential velocity was active in all cases, except for $B = 16$, $\eta_c = 0{\cdot}645$. The constraint for minimum chord length was active for $B = 4$, $\eta_c \geqslant 0{\cdot}56$ and for $B = 8$, $0{\cdot}58 \leqslant \eta_c \leqslant 0{\cdot}61$. Finally, the constraint for maximum $\Omega$ was active for $B = 4$, $\eta_c = 0{\cdot}565$, for $B = 8$, $\eta_c \geqslant 0{\cdot}61$, and for $B = 16$, $\eta_c \geqslant 0{\cdot}64$.

### 3.3. MINIMUM NOISE, FIXED HUB RADIUS

The trailing edge noise was minimized, excluding the hub radius from the design variables. Instead, the hub radius was altered in a parametric study. The flow rate was $Q = 4{\cdot}45\,\mathrm{m}^3/\mathrm{s}$ and two values of the pressure rise constraint were used, either $p_T = 2000$ or 2400 Pa. In both cases, $B = 16$ blades was used. Figure 8 depicts the minimum *SPL* as

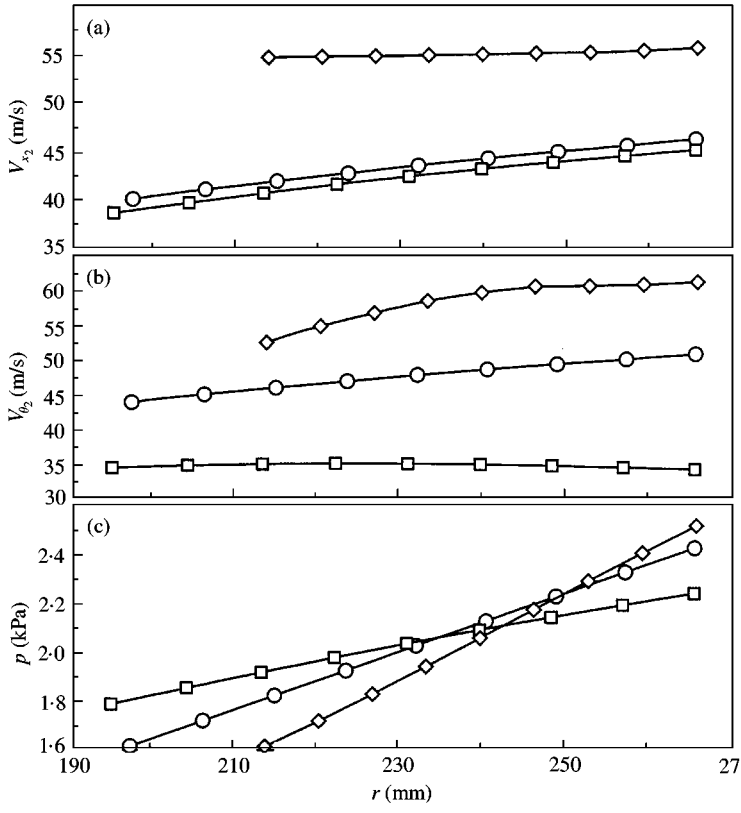


Figure 5. Spanwise distributions of axial velocity at the far downstream (a), tangential velocity at the far downstream (b), and static pressure rise across the fan (c) for the optimum designs, $B = 16$, $Q = 4{\cdot}45\,\mathrm{m}^3/\mathrm{s}$, $p_T = 2000\,\mathrm{Pa}$: ○, optimization for minimum $SPL$; □, optimization for maximum $\eta$; ◇, optimization for minimum $\Omega$.

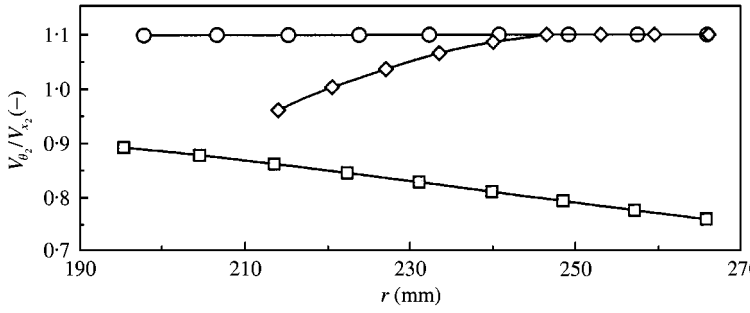


Figure 6. The spanwise distributions of the ratio of tangential-to-axial velocity in the outlet for the optimum designs, $B = 16$, $Q = 4{\cdot}45\,\mathrm{m}^3/\mathrm{s}$, $p_T = 2000\,\mathrm{Pa}$: ○, optimization for minimum $SPL$; □, optimization for maximum $\eta$; ◇, optimization for minimum $\Omega$.

a function of $r_h$. The left endpoint of each curve was the lowest $r_h$ for which a solution could be found. The right endpoint was chosen as $r_h = 0{\cdot}22\,\mathrm{m}$, but solutions were found for larger hub radii. The points marked "Opt" are from optimizations where $r_h$ was included as a design variable (as in section 3.1). The pressure rise constraint and the tangential velocity constraint were active in all cases.

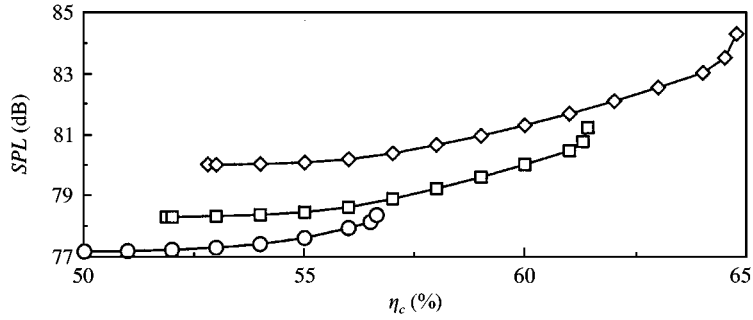


Figure 7. Minimum trailing edge noise with constraint on efficiency, $Q = 4{\cdot}45\,\mathrm{m}^3/\mathrm{s}$, $p_T = 2000\,\mathrm{Pa}$: ○, four blades; □, eight blades; ◇, 16 blades.

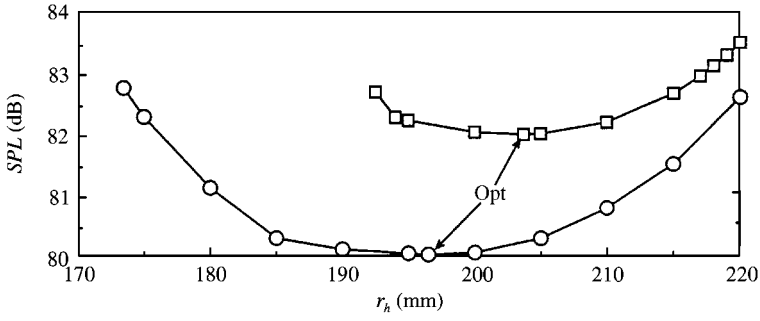


Figure 8. Minimum trailing edge noise as a function of hub radius, $Q = 4{\cdot}45\,\mathrm{m}^3/\mathrm{s}$, $B = 16$: ○, $p_T = 2000\,\mathrm{Pa}$; □, $p_T = 2400\,\mathrm{Pa}$. Points designated *Opt* are values found when $r_h$ was included as a design variable in the optimization.

## 4. DISCUSSION

Before discussing the results, some expectations of the optimizations, based on the governing equations for the aerodynamic model and for the trailing edge noise model, are given below. In the following, these are referred to as *Note* 1, etc.

*Note* 1. Since an optimization algorithm was used, the method of finding the "optimum" solution is strongly coupled. Thus, even though a change in one of the design variables could actually result in a poorer design if made alone, the optimization algorithm considers the combination of all design variables and thereby provides the "optimum" solution of the coupled problem.

*Note* 2. From equation (3) or Figure 1, it is seen that low values of $\Omega$ or large throughflow velocities (large $r_h$) result in small values of the angle $\beta$. To keep the airfoils of the blade elements in a high-performance setting, a small value of $\beta$ is accompanied by a small stagger angle in order to keep the angle of attack, $\alpha$, at a reasonable value.

*Note* 3. From equation (4), the *secondary drag* increases with increasing chord for fixed solidity. Thus, a rotor with many low-chord blades has a lower secondary drag than a rotor with few large-chord blades, neglecting effects from changes in Reynolds number. This means that the optimum designs are expected to have lower losses and thus increasing efficiencies for increasing number of blades.

*Note* 4. In the present study, the *tip clearance* was fixed at $t = 1\,\mathrm{mm}$ and the efficiency of the *downstream diffuser* was fixed at $\eta_D = 0{\cdot}95$. According to equations (5) and (6), losses due

to tip clearance and downstream diffuser both increase with increasing hub radius (since both $r_t - r_h$ and $A_1$ become smaller). Also, from equation (4), the secondary drag increases with increasing hub radius. Thus, a small hub radius is required for a high-efficiency fan. On the other hand, a very small hub radius results in low relative velocities at the inner part of the blade and the pressure rise requirement may be difficult to fulfill.

*Note* 5. According to equations (4) and (5), *secondary drag* losses and *tip clearance* losses increase with increasing lift coefficient of the blades. Thus, for a high efficiency fan, the lift coefficient must be low. At the same time, the pressure rise requirement must be met and for this to be possible, the rotational speed of the rotor must be high. Also, the aim of the optimization algorithm to lower the lift coefficient for all blade elements reduces the pressure rise at the inner part of the blade, resulting in a lower axial velocity in this region of the blade.

*Note* 6. Disregarding the small influence from $D_i$, the *total sound power* in equation (8) depends on the relative velocity $V_{rel,i}$ to the sixth power and the relative velocity must be small to minimize the *SPL*. Continuity imposes restrictions on the axial velocity, whereas the tangential velocity and the rotational speed of the rotor may vary freely within the constraints. According to equation (2), the tangential velocity will thus be large and the rotational speed of the rotor low in order to minimize $V_{rel,i}$. It is therefore expected that the constraint on the tangential velocity is active when optimizations are performed with the aim of minimizing the *SPL*. Since the dynamic pressure contained in the tangential velocity was not included in the pressure rise (section 2.1), the tangential velocity is regarded as an aerodynamical loss. Thus, the requirement of large tangential velocities for a low-noise fan results in low efficiencies. Alternatively, this may be stated as: the requirements of low tangential velocities for a high-efficiency fan result in a high *SPL*.

*Note* 7. From equation (8), the *SPL* is proportional to the number of blades, $B$ and, in each streamtube, proportional to the wake width, $D_i$. From equation (9), even with $D_T = 0$, $D_i$ is proportional to the chord to the power of 0·8 at the most. Therefore, the noise emission is generally lower for a rotor with few blades of large chord than for a rotor with many blades of small chord.

### 4.1. MINIMUM NOISE, MAXIMUM $\eta$ AND MINIMUM $\Omega$

In section 3.1, the optimization algorithm was used to determine three types of *optimum* fans, either (1) a fan with the lowest possible trailing edge noise (denoted min(*SPL*) in the following), (2) a fan with the highest possible efficiency (denoted max($\eta$)), or (3) a fan with the lowest possible rotational speed of the rotor (denoted min($\Omega$)).

As expected, the lower of the three curves in Figure 3(a) is the min(*SPL*) case since the optimizations for this case were performed with the specific aim of minimizing the *SPL*. The very high *SPL* for the max($\eta$) case may be explained by *Note* 6. For all cases, the *SPL* increased with increasing $B$, which agrees with *Note* 7. The upper curve in Figure 3(b) is the max($\eta$) case since the objective function in this case was to maximize the efficiency. The low efficiency of the min($\Omega$) case is because of the large hub radius (Figure 3(d)) and the limited degree of freedom to lower the losses (*Note* 4). For all curves, $\eta$ increased with increasing $B$, which is explained by *Note* 3. For the min(*SPL*) and min($\Omega$) cases, $\Omega$ decreased with an increase in the number of blades (Figure 3(c)), which corresponds to *Notes* 4 and 6. The max($\eta$) case has a constant value of $\Omega$, determined by the upper constraint value of 3000 r.p.m., which may be explained by *Note* 5. For the min(*SPL*) case, the hub radius was independent of the number of blades, whereas, for the cases of max($\eta$) and min($\Omega$), the hub radius increased with the number of blades (Figure 3(d)). The increase in hub radius which,

in itself, results in higher losses (*Note* 4) was due to the increased number of blades and thereby, decrease in the secondary loss (*Note* 3). This in turn increased the degree of freedom for the optimization algorithm, which then made a trade-off between the profile lift and drag characteristics and the additional losses respectively (*Note* 1). The hub radius for the min($\Omega$) case was much larger than for the min(*SPL*) and max($\eta$) cases, thereby increasing the throughflow velocity which, in turn, ensured a relative velocity, $V_{rel}$, which was large enough to provide the required pressure rise across the rotor.

From Figure 3, it is seen that there is a significant difference in the operating characteristics, depending on the chosen criterion for the "optimum" fan. As an example, consider $B = 16$ where the noise emission for the max($\eta$) case was approximately 4 dB larger than the min(*SPL*) case, whereas the efficiency for the max($\eta$) case was approximately 12 points larger than the min(*SPL*) case. The parametric study shown in Figure 3 may thus aid the design engineer toward the correct choice of fan-type, depending on the use of the fan. It must be emphasized that the above findings only apply to the noise generated at the trailing edges of the blades. Thus, the obtained results do not contradict the generally accepted belief that high-efficiency fans exhibit low overall noise characteristics [3].

For the selected case of $B = 16$, the cases of min(*SPL*) and max($\eta$) had similar chord lengths (Figure 4(a)), whereas the min($\Omega$) case had a much larger chord length to meet the pressure rise requirement, while minimizing the rotational speed of the rotor. For the min($\Omega$) case, a significant increase in chord length was followed by a decrease for large radii to prevent violation of the constraint on the tangential velocity (Figure 6). The stagger angle, $\xi$, was largest for the max($\eta$) case and smallest for the min($\Omega$) case (Figure 4(b)). The variation in stagger angle between the three cases is explained by *Note* 2, since the max($\eta$) case had the largest $\Omega$ and the lowest $r_h$, resulting in a large value of $\beta$ and thereby a large value of $\xi$, whereas the min($\Omega$) case had a small $\Omega$ and a large $r_h$, resulting in a small value of $\beta$ and thus a small value of $\xi$. For all three cases, the stagger angle increased with increasing radius since the product of radius and rotational speed of the rotor increased, thereby increasing $\beta$, and thus also $\xi$. The max($\eta$) case had the smallest camber angle and the min(*SPL*) case the largest camber angle (Figure 4(c)).

The axial velocities were almost identical for the min(*SPL*) and max($\eta$) cases (Figure 5(a)), whereas the min($\Omega$) case had a much larger axial velocity because of the large hub radius (and thereby large throughflow velocity). In all three cases, the axial velocity increased with increasing radius to keep a low lift coefficient (*Note* 5). For the corresponding tangential velocity, the max($\eta$) case had the lowest value (Figure 5(b)), whereby the aerodynamic loss was lowered (*Note* 6). Furthermore, the tangential-to-axial velocity ratio far downstream of the rotor was below the constraint value of 1.1 for all radii (Figure 6). The min($\Omega$) case had the highest tangential velocity because of the large axial velocity combined with a large tangential-to-axial velocity ratio (Figure 6) for which the corresponding constraint was active for most of the throughflow area. Otherwise, it would be possible to lower the rotational speed of the rotor even further and obtain the same pressure rise. Finally, the tangential velocity in the min(*SPL*) case was between the other two cases since the axial velocity was lower and the tangential velocity was determined by the constraint on the tangential velocity for all radii (Figure 6). All three cases had the same area-weighted mean value of the pressure rise from the imposed constraint, but the spanwise distributions differ significantly, with the smallest slope in the max($\eta$) case and the largest slope in the min($\Omega$) case (Figure 5(c)). This is because of the pressure equilibrium far downstream of the rotor (equation (1)), and the differences in the slopes are explained by the different magnitudes of the tangential velocities from Figure 5(b).

Section 3.1 contains a listing of the active constraints. The pressure rise constraint was active for all optimizations since a higher pressure limits the degree of freedom for the

optimization algorithm to improve the objective function. For the max($\eta$) case, the constraint on $\Omega$ was active (*Note* 5). The constraint on the tangential velocity was active for the min(*SPL*) and min($\Omega$) cases, according to the discussion of the tangential velocity distribution, given previously.

### 4.2. MINIMUM NOISE, CONSTRAINING $\eta$

In section 3.2, the optimization algorithm was used to determine the minimum trailing edge noise, while imposing a constraint on the efficiency to be above a specified level. This enabled an investigation of the trade-off between noise emission and efficiency for different numbers of blades as shown in Figure 7. For all three curves, the *SPL* increased with increasing $\eta_c$, since larger $\eta_c$ impose further requirements on the design, thereby lowering the degree of freedom to minimize the *SPL*. Also, the *SPL* increased with an increase in the number of blades which is in agreement with *Note* 7. Finally, the largest possible value of $\eta_c$ increased with the number of blades in accordance with *Note* 3.

Section 3.2 also contains the active constraints for the optimizations. In accordance with *Note* 6, the tangential velocity constraint was active in almost all cases. The constraint for $\eta_c$ was always active since it was given a value above the value determined in section 3.1, where no constraint was imposed on the efficiency. For large values of $\eta_c$, for the three curves, the constraint on $\Omega$ became active in order to obtain the high efficiency (*Note* 5). Finally, in a few cases, other constraints were active as well.

### 4.3. MINIMUM NOISE, FIXED HUB RADIUS

In section 3.3, the optimizations were carried out for fixed values of the hub radius, which was thus excluded as a design variable. Knowledge of the dependency of the trailing edge noise on the size of the hub radius may be of significance if a limited number of *standard* motor/hub modules are available for fan assembly.

From Figure 8, the case of $p_T = 2000$ Pa had a lower level of *SPL* than the case of $p_T = 2400$ Pa because the lower pressure rise requirement resulted in a lower rotational speed of the rotor (*Note* 6). Also, the hub radius for which the lowest possible *SPL* was found (marked with "Opt" in Figure 8), was lower for the case of $p_T = 2000$ Pa than for the case of $p_T = 2400$ Pa because a lower pressure rise can be obtained with a lower relative velocity which, in turn, requires a lower throughflow velocity and thereby a smaller hub radius. Finally, Figure 8 may aid the fan designer in choosing a reasonable *standard* hub radius, for a given pressure rise duty of the fan, in order to keep the trailing edge noise low.

## 5. CONCLUSIONS

Models for the trailing edge noise and aerodynamics of arbitrary vortex flow fans were successfully combined into an analysis tool for fan performance, as well as for trailing edge noise. This model was then combined with a standard method for numerical design optimization of constrained non-linear problems, which thereby enabled the design of low-noise fans at user-defined flow rate and pressure rise duty. The chosen design variables included rotational speed of the rotor, hub radius, and spanwise distributions of chord, stagger, and camber angle. Constraints were imposed to ensure non-stalled conditions as well as geometrical and operational requirements.

Optimizations showed that large differences existed in trailing edge noise, efficiency, and other characteristics of the fan, depending on whether the fan was optimized for minimum trailing edge noise, maximum efficiency, or minimum rotational speed of the rotor. Also, by constraining the efficiency above a given value, a significant increase in fan efficiency was possible with only a limited increase in trailing edge noise. Finally, a parametric study of the dependence of the trailing edge noise on the hub radius showed that an interval of hub radii existed for which the trailing edge noise was almost constant.

## ACKNOWLEDGMENTS

The work was partly supported by the Danish Energy Agency under contract No. 1253/96-0002.

## REFERENCES

1. P. E. DOAK and P. G. VAIDYA 1969 *Journal of Sound and Vibration* **9**, 192–196. A note on the relative importance of discrete frequency and broad-band noise generating mechanisms in axial fans.
2. N. LE S. FILLEUL 1966 *Journal of Sound and Vibration* **3**, 147–165. An investigation of axial flow fan noise.
3. T. FUKANO, Y. TAKAMATSU and Y. KODAMA 1986 *Journal of Sound and Vibration* **105**, 291–308. The effects of tip clearance on the noise of low pressure axial and mixed flow fans.
4. T. FUKANO, Y. KODAMA and Y. TAKAMATSU 1980 *Bulletin of the JSME* **23**, 1335–1343. Discrete frequency noise due to irregularity in blade row of axial fan rotor.
5. R. E. LONGHOUSE 1976 *Journal of Sound and Vibration* **48**, 461–474. Noise mechanism separation and design considerations for low tip-speed, axial-flow fans.
6. I. J. SHARLAND 1964 *Journal of Sound and Vibration* **1**, 302–322. Sources of noise in axial flow fans.
7. T. FUKANO, Y. KODAMA and Y. SENOO 1977 *Journal of Sound and Vibration* **50**, 63–74. Noise generated by low pressure axial flow fans. I: Modeling of the turbulent noise.
8. R. E. LONGHOUSE 1977 *Journal of Sound and Vibration* **53**, 25–46. Vortex shedding noise of low tip speed, axial flow fans.
9. D. N. SØRENSEN, M. C. THOMPSON and J. N. SØRENSEN 2000 *American Society of Mechanical Engineers Journal of Fluids Engineering* **122**, 324–329. Toward improved rotor-only axial fans—Part II: Design optimization for maximum efficiency.
10. T. FUKANO, Y. KODAMA and Y. TAKAMATSU 1977 *Journal of Sound and Vibration* **50**, 75–88. Noise generated by low pressure axial flow fans. II: effects of number of blades, chord length and camber of blade.
11. T. FUKANO, Y. KODAMA and Y. TAKAMATSU 1978 *Journal of Sound and Vibration* **56**, 261–277. Noise generated by low pressure axial flow fans. III: effects of rotational frequency, blade thickness and outer blade profile.
12. C. LEE, M. K. CHUNG and Y.-H. KIM 1993 *Journal of Sound and Vibration* **164**, 327–336. A prediction model for the vortex shedding noise from the wake of an airfoil or axial flow fan blades.
13. D. N. SØRENSEN and J. N. SØRENSEN 2000 *American Society of Mechanical Engineers Journal of Fluids Engineering* **122**, 318–323. Toward improved rotor-only axial fans-part. I: a numerically efficient aerodynamic model for arbitrary vortex flow.
14. X. YANG and N. NIE 1986 in 1986 *International Conference of Noise Control Engineering. Inter-noise* 86, (R. Lotz, editor), 175–180. Noise control foundation. The optimum low noise flow-type of low pressure axial flow fans.
15. J. C. EMERY, J. R. HERRIG and A. R. FELIX 1958 *Report TR*-1368, *NACA*, *Langley Aeronautical Laboratory*, *Langley Field*, *VA*. Systematic two-dimensional cascade tests of NACA 65-series compressor blades at low speeds.
16. R. A. WALLIS 1993 *Axial Flow Fans and Ducts*. Malabar, FL: Krieger Publishing Company.
17. B. LAKSHMINARAYANA and J. H. HORLOCK 1967 *Report R & M* 3483, *British Aeronautical Research Council*. Leakage and secondary flow in compressor cascades.

18. S. A. L. GLEGG and C. JOCHAULT 1998 *American Institute of Aeronautics and Astronautics Journal* **36**, 1387–1395. Broadband self-noise from a ducted fan.
19. J. LAVRENTJEV and M. ÅBOM 1996 *Journal of Sound and Vibration* **197**, 1–16. Characterization of fluid machines as acoustic multi-port sources.
20. S. P. HAN 1976 *Mathematical Programming* **11**, 263–282. Superlinearly convergent variable metric algorithms for general nonlinear programming problems.
21. M. J. D. POWELL 1978 *Mathematical Programming* **14**, 224–248. Algorithms for nonlinear constraints that use Lagrangian functions.
22. D. N. SØRENSEN 1998 *Thesis ET-PHD* 9801, *Department of Energy Engineering, Technical University of Denmark*. Aerodynamic modelling and optimization of axial fans.

## APPENDIX A: NOMENCLATURE

| | |
|---|---|
| $A_1$ | annulus area |
| $A_2$ | duct area |
| $a_0$ | speed of sound |
| $B$ | number of blades |
| $c$ | chord |
| $C_{D_s}$ | secondary drag term |
| $C_{D_{tip}}$ | tip loss term |
| $\bar{C}_L$ | average lift coefficient |
| $d$ | distance from the rotor to the noise measuring probe |
| $D$ | wake width behind airfoil |
| $D_T$ | airfoil trailing edge width |
| $f$ | frequence of trailing edge noise |
| $E$ | total sound power radiated from the rotor |
| $F$ | objective function (figure of merit) |
| $g_j$ | constraint no. $j$ |
| $N$ | number of annular control volumes |
| $NCON$ | number of constraints |
| $NDV$ | number of design variables |
| $P$ | mechanical shaft power |
| $p$ | static pressure |
| $p_0$ | static pressure level |
| $\Delta p_D$ | pressure loss in downstream diffuser |
| $p_{ref}$ | reference pressure in $SPL$ |
| $p_T$ | integrated fan pressure rise |
| $Q$ | flow rate |
| Re | Reynolds number based on $c$ and $V_{rel}$ |
| $r$ | radius |
| $r_h$ | hub radius |
| $r_t$ | tip radius |
| $s$ | interblade spacing, $s = 2\pi r/B$ |
| $SPL$ | overall sound pressure level |
| St | Strouhal number based on $D$, $f$ and $V_{rel}$ |
| $t$ | tip clearance height |
| $V_{rel}$ | velocity relative to blade element |
| $V_x$ | axial velocity |
| $V_\theta$ | tangential velocity |
| $w$ | axially induced velocity |
| $w_0$ | constant level of the axially induced velocity |
| $\alpha$ | angle of attack on airfoil, $\alpha = \beta - \xi$ |
| $\beta$ | angle between rotational axis and $V_{rel}$ |
| $\eta$ | fan efficiency |
| $\eta_c$ | constraint value imposed on $\eta$ |
| $\eta_D$ | efficiency of downstream diffuser |
| $\Omega$ | rotational speed of the rotor |
| $\Phi_n$ | design variable no. $n$ |

$\rho$ density of fluid
$\sigma$ solidity, $\sigma = c/s$
$\theta$ camber angle
$\xi$ stagger angle

*Subscripts*

$(\cdot)_1$ plane far upstream of the rotor disc
$(\cdot)_d$ plane at the rotor disc
$(\cdot)_2$ plane far downstream of the rotor disc
$(\cdot)_i$ stream tube no. $i$